

Torus-Projected Electromagnetic Wormholes Enabled by Anisotropic Singularity Reconstruction of Metamaterials

Junke Liao¹†, Wen Xiao¹†, Yixiao Ge¹, Huanyang Chen¹*

¹Department of Physics, Xiamen University; Xiamen 365100, China.

†These authors contributed equally to this work

*Corresponding author. Email: kenyon@xmu.edu.cn

Abstract: Transformation optics uses coordinate mappings to emulate curved geometries and control electromagnetic fields. However, existing approaches primarily focus on geometric deformation while offering limited control over the global topology of the resulting optical space. Here we introduce a torus projection combined with a conformal mapping to construct a wormhole-like virtual optical geometry, providing a controllable route to manipulate optical-space topology within transformation optics. By tuning a single torus parameter, the virtual-space refractive index switches between isotropic and anisotropic forms, transforming point-like singularities in a disconnected geometry into extended transport channels that connect the optical space. This topology transition manifests as the opening or closure of an electromagnetic wormhole and is accompanied by pronounced changes in ray dynamics and cavity modes. Our results demonstrate how refractive-index anisotropy governs singularity structure and topology in transformation optics, providing a route to photonic systems with tunable optical geometry and connectivity.

Introduction

Transformation optics (TO) [1,2] provides a unified framework linking electromagnetic field control to spacetime geometry through coordinate transformations [4-7]. This approach enables the design of materials that mimic gravitational effects, giving rise to analogs of phenomena such as black holes [8,9] and gravitational lenses [10]. Beyond reproducing known astrophysical metrics, TO offers a route to emulate theoretical spacetime constructs predicted by general relativity. Among these, the Einstein–Rosen bridge, or wormhole, represents a geometry connecting two black holes through a nontrivial topology [11,12]. TO-based analogs of such “wormhole-like” systems have been demonstrated as invisible electromagnetic tunnels [13] and embedded two-dimensional surfaces [14,15], capturing essential geometric and field properties. However, these realizations remain confined to disconnected configurations without a controllable linkage between spatially separated black holes, which represents a key step toward realizing physically meaningful wormhole analogs with tunable electromagnetic properties. This motivates a deeper question: can one construct, in flat space, an equivalent geometry that connects two black holes while keeping them separate, and whose “singularity” can be opened or closed with observable electromagnetic effect?

In this work, we construct a ring-shaped electromagnetic wormhole in virtual space by combining a conformal mapping hosting dual black-hole–like singularities with a torus projection. This construction allows the geometry of the virtual optical space to be continuously tuned while maintaining spatial separation in physical space. As the torus parameters are varied, the refractive-index distribution in virtual space switches between isotropic and anisotropic forms, leading to distinct optical geometries. We show that anisotropy in transformation optics can fundamentally reconstruct optical singularities, converting point-like defects into extended transport channels and inducing a topological transition of the effective optical space. During this singularity transition, black-hole-like effects [16–18] emerge within the wormhole, and the cavity modes evolve from a uniform intensity profile to alternating light–dark stripes, driven by an underlying change in topology. This transition alters light propagation and cavity modes, highlighting the pivotal role of refractive index anisotropy in shaping the topology of wormhole geometries.

Conformal mapping with dual black holes

We begin by examining the optical space generated by a logarithmic conformal transformation, which gives rise to two singular points that act as black-hole–like absorbers for light [19]:

$$w(z) = z + \alpha(\ln(z + \beta) - \ln(z - \beta)). \quad (1)$$

where $w = u + iv$ represents the coordinates in virtual space, $z = x + iy$ represents the coordinates in physical space, α and β are parameters of this transformation. This conformal transformation incorporates two logarithmic terms and a linear term. With finite values of α and β , this mapping ensures $w(z) = z$ at infinity, introducing two singularities in the physical space at locations $z = \beta$ and $z = -\beta$.

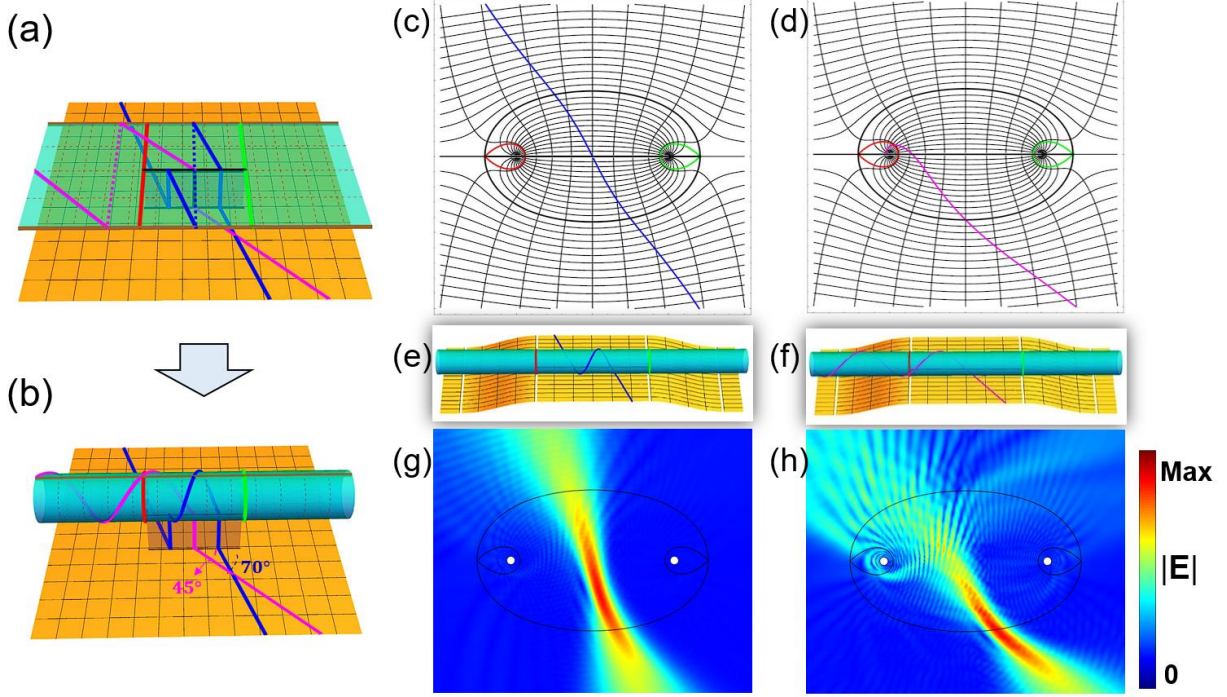


Fig 1. The virtual and physical spaces of the conformal transformation with dual black holes. (a) and (b) depict the two behaviors of light rays in the virtual space. The existence of periodic boundary conditions makes the upper Riemann sheet equivalent to a cylindrical surface. (c) and (d) illustrate the ray tracing of two scenarios in the physical space. (e) and (f) show the virtual space for $\alpha = 0.5$ and $\beta = 1$. (g) and (h) show simulations of a Gaussian beam with $\lambda = 0.1$ in the physical space. The black bold oval in the z plane correspond to the branch cut in (a) and (b). The interior of this circle relates to the upper Riemann sheet of the virtual space, while the exterior corresponds to the lower Riemann sheet.

As illustrated in Fig. 1(a), the virtual space consists of two Riemann sheets connected by a branch cut. The lower sheet is unbounded in both directions, whereas the upper sheet is finite in the transverse direction and periodic along its boundaries. This periodicity renders the upper Riemann sheet topologically equivalent to a cylinder, allowing light rays to circulate indefinitely once they enter this sheet [20]. In virtual space, light interacting with the branch cut exhibits two qualitatively distinct dynamical behaviors, depending on its incident direction. For certain small angles, rays cross the branch cut, temporarily access the cylindrical sheet, and subsequently return to the lower sheet, preserving global propagation, as shown by the blue lines in Fig. 1(a) and Fig. 1(b). In contrast, for small incident angles, rays are redirected toward the black hole boundaries (red and green circles) of the cylindrical sheet, where they propagate indefinitely and never return to the lower sheet as shown by the magenta lines in Fig. 1(a) and Fig. 1(b).

This virtual-space dynamics is directly inherited by physical space. Hamiltonian ray tracing [21,22] confirms that rays in physical space either complete a closed excursion on the upper Riemann sheet and re-emerge into the lower sheet, or are permanently captured by the singularities, faithfully reflecting the cylindrical topology of the virtual space (Figs. 1(c) and 1(d)). Full-wave simulations of transverse-electric (TE) Gaussian beams ($\lambda = 0.1$, $\alpha = 0.5$, $\beta = 1$) further confirm this behavior, showing that waves either traverse the branch cut or are predominantly captured by the singularities (Figs. 1(g) and 1(h)). Overall, this logarithmic conformal transformation naturally

generates a pair of optical black holes, whose capture and transmission properties are consistently described by virtual-space topology, Hamiltonian ray dynamics, and full-wave simulations.

Torus Projection

To go beyond isolated optical black holes, we now examine how the topology of the virtual space can be fundamentally altered. The key idea is to reconnect the two asymptotic ends of the cylindrical Riemann sheet, thereby transforming a pair of disconnected infinities into a single, multiply connected manifold. This reconnection is achieved through a toroidal projection, inspired by the role of stereographic projection in Maxwell's fisheye lens [23,24]. While stereographic projection maps a closed spherical surface onto a plane, the torus projection maps a closed toroidal surface onto a cylindrical space, as shown in Fig. 2(a-d). In doing so, it introduces a geometric throat that links the two ends of the cylinder, which previously corresponded to independent black holes.

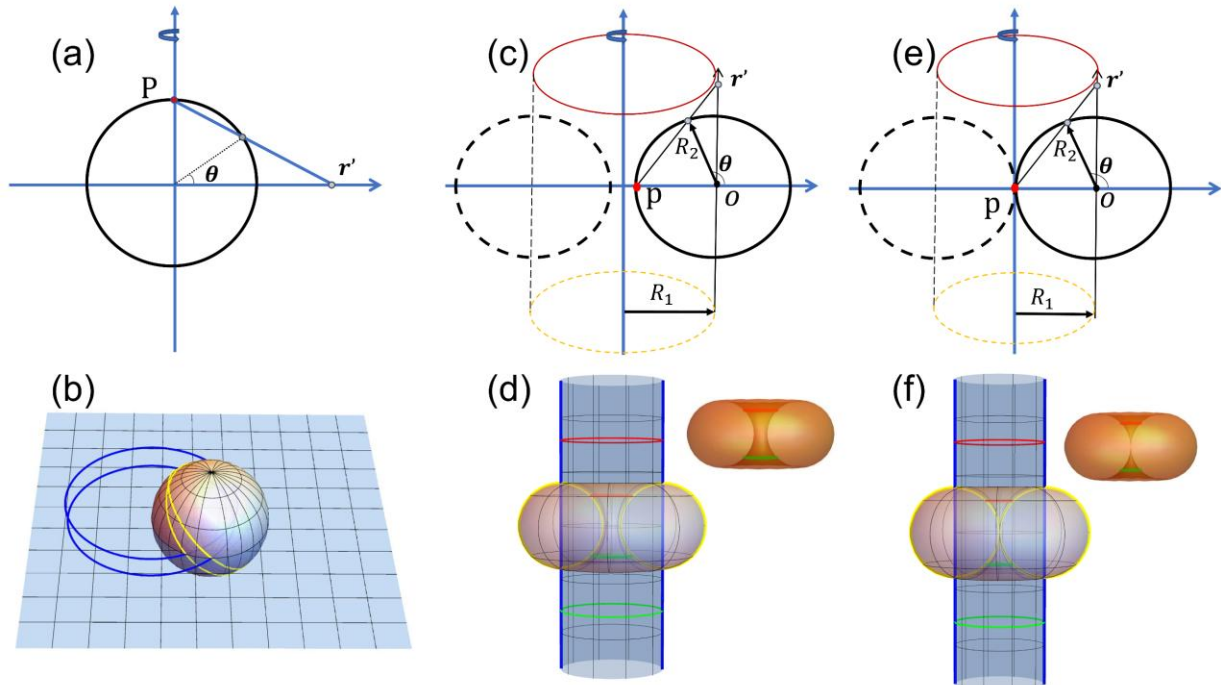


Fig 2. stereographic and torus projections. (a) Cross-sectional view of the stereographic projection. (b) Projection trajectories (blue lines) of geodesics on the circle (yellow lines) under spherical projection. (c) Cross-sectional view of the ring torus projection. (e) Cross-sectional view of the horn torus projection. (d) and (f) show the projection trajectories on the cylindrical surface, respectively. The red and green circles represent the two black holes in the conformal mapping with dual black holes.

We now provide a detailed description of the torus projection. A torus is characterized by two radii: the major radius R_1 and the minor radius R_2 . As illustrated in Fig. 2(c), a torus can be generated by rotating a circular cross-section of radius R_2 around a central axis located at a distance R_1 , in a manner analogous to the formation of a sphere by rotating a circle. Similarly, we identify a projection point P on this toroidal cross-section and project all points from the surface of the ring torus, with a major radius of R_1 and a minor radius of R_2 , onto the cylindrical surface with a radius of R_1 . In cylindrical coordinates (r', φ') , the mapping reads

$$\begin{cases} r' = R_2 \frac{\sin(\theta)}{\cos(\theta) + 1} \\ \varphi' = \varphi \end{cases} \quad (2)$$

where r' represents the axial parameter of the cylindrical surface. The metric on the torus is given by $ds^2 = R_2^2 d\theta^2 + (R_1 + R_2 \cos(\theta))^2 d\varphi^2$, while the metric on the cylindrical surface with anisotropic refractive index distribution can be expressed as

$$ds'^2 = n_{r'}^2 dr'^2 + n_{\varphi'}^2 R_1^2 d\varphi'^2 \quad (3)$$

We apply the torus projection mapping to the metric of the toroidal surface with anisotropic refractive index distribution:

$$ds'^2 = n_{r'}^2 R_2^2 \frac{1}{(1 + \cos(\theta))^2} d\theta^2 + n_{\varphi'}^2 R_1^2 d\varphi'^2 \quad (4)$$

To replicate the trajectory from a toroidal surface onto a cylindrical surface, we can obtain $n_{r'} = 1 + \cos(\theta) = 1 + \frac{R_2^2 - r'^2}{R_2^2 + r'^2}$ and $n_{\varphi'} = 1 + \frac{R_2}{R_1} \cdot \cos(\theta) = 1 + \frac{R_2}{R_1} \cdot \frac{R_2^2 - r'^2}{R_2^2 + r'^2}$.

From a physical standpoint, this projection does not merely reshape trajectories but reconstructs the global connectivity of optical space. The upper Riemann sheet, which originally terminated at two singular endpoints, is converted into a closed surface supporting non-contractible loops. As a result, light that would otherwise be absorbed at a black hole can now circulate through the toroidal manifold. By applying torus projection and imposing the torus's refractive index distribution onto the cylindrical surface within the virtual space of the conformal transformation [25,26], dual black holes can be interconnected, forming what we term a ring wormhole. Notably, when varying the geometric parameters R_1 and R_2 of the torus, the ring torus degenerates into a horn torus when $R_1 = R_2$. In this limit, the throat of the ring wormhole collapses to a point, restoring the disconnection between the two asymptotic regions, as shown in Figs. 2(e) and 2(f). This situation is similar to the closure of the Einstein-Rosen bridge. Remarkably, when $R_1 = R_2$, the cylindrical refractive index distribution becomes isotropic, coinciding exactly with the throat's closure.

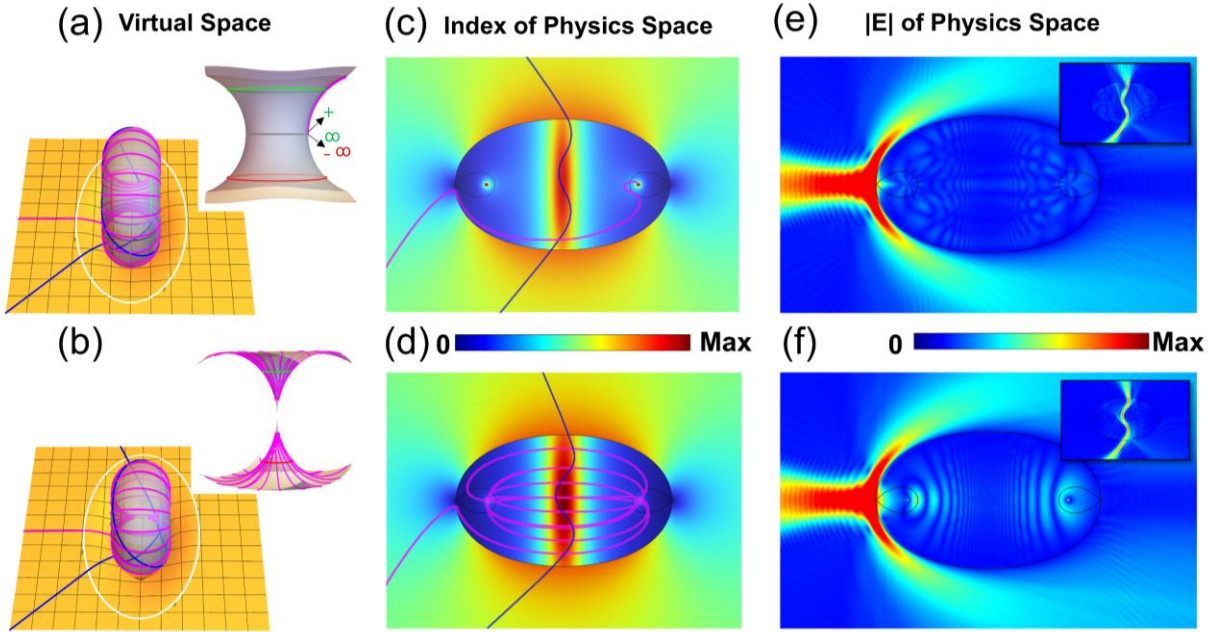


Fig. 3. Construction and electromagnetic realization of a torus-projected wormhole. (a,b) Ray trajectories in virtual space for $c = 2/3$ (open wormhole) and $c = 1$ (closed wormhole). (c,d)

Corresponding ray trajectories and refractive-index distributions in physical space. (e,f) Full-wave simulations under Gaussian-beam excitation, confirming the consistency between ray dynamics and wave behavior.

Electromagnetic Wormhole

We define the ratio $\frac{R_2}{R_1}$ as c , which controls the geometry of the torus and, consequently, the topology of the projected cylindrical space. Therefore, the refractive index on the cylinder in virtual space can be written as:

$$n_{r'} = 1 + \frac{c^2 \alpha^2 - r'^2}{c^2 \alpha^2 + r'^2}, \quad n_{\varphi'} = 1 + c \cdot \frac{c^2 \alpha^2 - r'^2}{c^2 \alpha^2 + r'^2} \quad (5)$$

where the anisotropy explicitly depends on the parameter c . When $c = 1$, the torus degenerates into a horn torus and the refractive index in virtual space becomes isotropic, satisfying $n_{r'} = n_{\varphi'}$. In this limit, radial and angular directions are equivalent up to a local scale factor, and the virtual-space geometry preserves conformal symmetry. Consequently, the transport channel collapses into an isolated singular point, and the two asymptotic ends of the cylindrical space remain disconnected. In contrast, when $c < 1$, the torus projection introduces an intrinsic anisotropy into the virtual-space metric, leading to $n_{r'} \neq n_{\varphi'}$. This anisotropy breaks the conformal symmetry of the virtual space: radial and angular directions are no longer equivalent, and scale-rotation covariance is lost. As a result, the optical singularities are no longer point-like terminations. Instead, they are geometrically reconstructed into an extended transport channel that connects the two asymptotic ends of the virtual cylindrical space, enabling a nontrivial wormhole-like topology. Therefore, the wormhole can be continuously opened or closed by tuning the parameter c , which controls the anisotropy of the virtual-space metric. This tuning realizes a topological transition between distinct toroidal geometries—from a horn torus with disconnected asymptotic regions to a ring torus with a connected transport channel—thereby providing a controllable on–off switching mechanism for the electromagnetic wormhole.

In our case, r' is the axial coordinate of the cylinder, corresponding to the u -direction in the conformal transformation with dual black holes. Thus, the refractive index for the cylinder can be expressed as:

$$n_{r'} = 1 + \frac{c^2 \alpha^2 - u^2}{c^2 \alpha^2 + u^2}, \quad n_{\varphi'} = 1 + c \cdot \frac{c^2 \alpha^2 - u^2}{c^2 \alpha^2 + u^2} \quad (6)$$

The corresponding refractive index distribution in physical space is more complex, and the detailed derivation and expression can be found in Appendix A.

The effect of this topology control is first illustrated in virtual space, as shown in Figs. 3(a) and 3(b). For $c = 2/3$, ray trajectories traverse the entire toroidal surface, connecting one asymptotic region to the other and forming a continuous transport path. For $c = 1$, the wormhole throat closes and rays no longer cross the singularities, indicating that the two asymptotic regions remain disconnected. The corresponding ray trajectories and refractive-index distributions in physical space are shown in Figs. 3(c) and 3(d). When $c < 1$, rays entering the structure are trapped near the black-hole singularities in physical space, even though in virtual space they remain globally connected. This apparent trapping does not correspond to true absorption of light but arises from the torus projection itself: when $c < 1$, ray trajectories that traverse the interior of the ring undergo an infinity-to-infinity transition in virtual space, which cannot be faithfully represented on the cylindrical surface (detailed information in Appendix B). As a result, these globally connected trajectories are projected into physical space as rays that accumulate near a

single singularity, giving rise to the appearance of black-hole trapping. When $c = 1$, this misalignment vanishes: rays oscillate between the two singularities without forming a connecting channel, consistent with a closed wormhole geometry. Full-wave simulations of Gaussian-beam excitation, shown in Figs. 3(e) and 3(f), further validate this picture. For $c < 1$, petal-shaped intensity patterns and cavity-like field distributions emerge, indicating continuous circulation through the virtual-space ring. If the singularities were isolated, such cavity modes would not persist. When $c = 1$, the black-hole-like trapping effect disappears, while the cavity mode evolves into a more regular distribution, reflecting the closure of the wormhole throat. Together, Fig. 3 demonstrates how anisotropy introduced by torus projection reconstructs the optical singularities and enables a topological transition of the effective optical space, realizing an electromagnetic wormhole that is connected in virtual space while remaining separated in physical space.

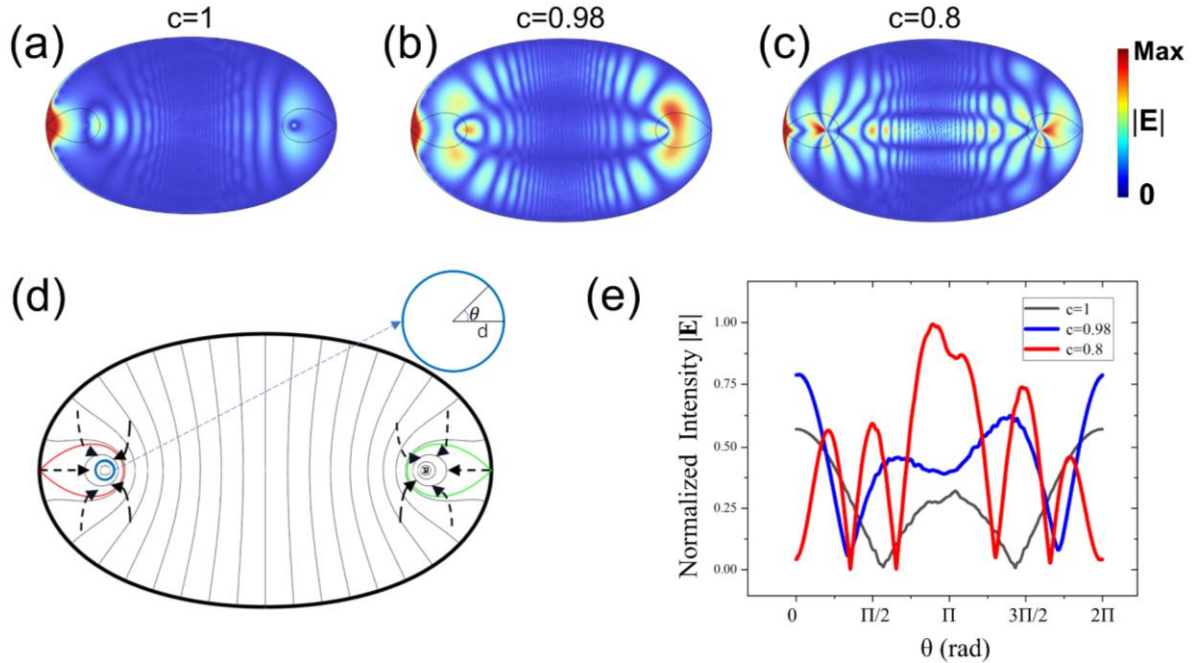


Fig. 4. Evolution of cavity modes and singularity reconstruction induced by anisotropy. (a–c) Steady-state cavity modes for $c = 1$, 0.98, and 0.8 excited by a Gaussian beam ($\lambda = 0.2$). (d) Schematic illustration of the field-pattern evolution as c decreases. (e) Normalized electric-field intensity $|E|$ sampled along a circular path (radius $d = 0.1$) around one singularity. The number of intensity peaks reflects the angular structure of the reconstructed singularity. As c decreases, the enhanced $|E|$ accumulation indicates strengthened gravitational-lensing effects.

To further reveal how anisotropy reconstructs optical singularities and alters the effective topology of the optical space, we examine the evolution of cavity modes for $c = 1$, 0.98, and 0.8, as shown in Fig. 4. When $c = 1$, the refractive index is isotropic and the virtual space corresponds to a horn-torus geometry. The optical singularities remain point-like, and the cavity mode exhibits a relatively uniform field distribution with weak angular modulation (Fig. 4(a)). In this regime, light is primarily localized near the singular points, consistent with a closed wormhole throat and disconnected asymptotic regions.

As c decreases below unity, anisotropy is introduced into the virtual-space metric, leading to a qualitative reconstruction of the singularities. The electromagnetic field no longer concentrates at isolated points; instead, it develops pronounced angular structure around each singularity, forming petal-like intensity patterns (Figs. 4(b, c)). The corresponding increase in $|E|$ near the

singularities, quantified in Fig. 4(e), indicates enhanced gravitational-lensing effects and stronger light bending.

Simultaneously, the global cavity mode undergoes a topological transformation. The field distribution evolves from a uniform pattern into alternating stripes extending across the cavity, reflecting interference supported by the newly formed extended transport channel in virtual space. Notably, the transition is highly sensitive near $c \approx 1$: a small deviation from isotropy ($c = 0.98$) already produces a marked change in both angular structure and cavity pattern, signaling the topological transition from a horn torus to a ring torus. Further reductions in c increase the number of stripes, corresponding to more complex wave circulation enabled by the reconstructed singular geometry.

These observations demonstrate that anisotropy in transformation optics does not merely modify field distributions quantitatively. Instead, it fundamentally reconstructs optical singularities from point-like defects into extended angular structures, enabling global light transport and inducing a topological transition of the effective optical space.

Conclusion

In this work, we have proposed an electromagnetic wormhole based on a torus projection within the framework of transformation optics, in which two black-hole-like singularities remain spatially separated in physical space while becoming topologically connected in virtual space. Beyond the construction of a specific wormhole geometry, our results reveal a geometric mechanism by which anisotropy reconstructs optical singularities and induces a topological transition of the effective optical space. By tuning a single parameter c , the virtual-space metric evolves from an isotropic, conformally symmetric horn-torus geometry to an intrinsically anisotropic ring-torus geometry. This transition breaks the equivalence between radial and angular directions, converts point-like singular terminations into extended transport channels, and changes the global connectivity of the virtual cylindrical space. Within this mechanism, the opening and closure of the wormhole correspond to a genuine topological transition rather than a local geometric deformation. The associated changes in ray dynamics and cavity modes—ranging from uniform field distributions to stripe-like and petal-shaped patterns—provide direct electromagnetic signatures of singularity reconstruction and topology switching.

Our work establishes that anisotropy in transformation optics is not merely a quantitative modification of refractive index, but a fundamental geometric degree of freedom capable of controlling singularity structure and global topology. This insight offers a new paradigm for designing electromagnetic wormholes and, more broadly, for engineering optical spaces with tunable topology, opening new possibilities for manipulating light transport, cavity dynamics, and singularity-driven phenomena in photonic systems.

Appendix A. Refractive index of the wormhole in physical space

When integrating the conformal transformation with the torus projection to form a wormhole, additional complexities must be addressed. Firstly, parameters α in the conformal transformation govern the period in the upper Riemann sheet, which corresponds to the radius of the cylindrical surface. The main radius R_1 of the projected torus must be equal to α in conformal transformation. Secondly, the calculation of the refractive index distribution in conformal transformations, given by $n = n_w |\frac{dw}{dz}|$, satisfies the Cauchy-Riemann conditions if and only if the refractive index

distribution n_w in the virtual space is isotropic. If n_w is anisotropic in the virtual space, this formula is no longer applicable, and a general coordinate transformation is required to compute the corresponding refractive index distribution in the physical space.

To begin with, we examine the simplified case of a horn wormhole, where $c=1$, yielding $n_{r'} = n_{\phi'} = \frac{2\alpha^2}{\alpha^2 + u^2}$. Due to the isotropic material distribution in the virtual space, we can straightforwardly apply the formula $n = n_w |\frac{dw}{dz}|$ to obtain an isotropic refractive index distribution in the physical space:

$$n_{in} = \frac{2\alpha^2}{\alpha^2 + u^2} \cdot \left| \frac{\beta^2 + 2\alpha\beta - z^2}{\beta^2 - z^2} \right| \quad (A1)$$

where $z = x + iy$ and $u = x + \frac{\alpha}{2} * \ln \left(\frac{(x+1)^2 + y^2}{(x-1)^2 + y^2} \right)$ as determined by the conformal transformation.

The refractive index distribution outside the wormhole is given by:

$$n_{out} = \left| \frac{\beta^2 + 2\alpha\beta - z^2}{\beta^2 - z^2} \right| = \frac{\sqrt{(\beta^2 + 2\alpha\beta - x^2 + y^2)^2 + 4x^2y^2}}{\sqrt{(\beta^2 - x^2 + y^2)^2 + 4x^2y^2}} \quad (A2)$$

In the main text, we set $\alpha=0.5$ and $\beta=1$ to align with the previous dual black hole simulation. The refractive index of a ring wormhole is not isotropic, making the calculations more complex. Firstly, in virtual space, the line element of a cylindrical surface is:

$$ds'^2 = n_{r'}^2 dr'^2 + n_{\phi'}^2 R_1^2 d\phi'^2 \quad (A3)$$

Given $dr' = du$ and $R_1 d\phi = dv$, the line element in virtual space can also be expressed in terms of u and v as:

$$ds'^2 = n_{r'}^2 du^2 + n_{\phi'}^2 dv^2 \quad (A4)$$

However, to achieve a material realization in physical space that replicates the same form of the line element as in virtual space, we need to determine the metric tensor form in physical space and subsequently derive the corresponding electromagnetic parameters. In physical space, the line element is expressed as:

$$ds'^2 = n_{uv} dx^u dx^v \quad (A5)$$

The transformation between the coordinates of physical and virtual space is determined by the conformal transformation equation:

$$\begin{cases} u = x + \frac{\alpha}{2} \cdot \ln \left(\frac{(x + \beta)^2 + y^2}{(x - \beta)^2 + y^2} \right) \\ v = y + \alpha \cdot \left(\text{Pi} + \tan^{-1} \left(\frac{y}{x + \beta} \right) - \tan^{-1} \left(\frac{y}{x - \beta} \right) \right) \end{cases} \quad (A6)$$

From simple coordinate substitutions, we know:

$$ds'^2 = \left(n_{r'}^2 \cdot \left(\frac{\partial u}{\partial x} \right)^2 + n_{\phi'}^2 \cdot \left(\frac{\partial v}{\partial x} \right)^2 \right) dx^2 + 2 \left(n_{r'}^2 \cdot \left(\frac{\partial u}{\partial x} \right) \left(\frac{\partial u}{\partial y} \right) + n_{\phi'}^2 \cdot \left(\frac{\partial v}{\partial x} \right) \left(\frac{\partial v}{\partial y} \right) \right) dxdy + \left(n_{r'}^2 \cdot \left(\frac{\partial u}{\partial y} \right)^2 + n_{\phi'}^2 \cdot \left(\frac{\partial v}{\partial y} \right)^2 \right) dy^2 \quad (S13)$$

By substituting Eq. (A6) into the above expression, we can obtain the refractive index distribution in physical space.

$$n = \begin{bmatrix} n_{xx} & n_{xy} & \square \\ n_{xy} & n_{yy} & \square \\ \square & \square & 1 \end{bmatrix} \quad (A7)$$

$$n_{xx} = \frac{16x^2y^2\alpha^2((-1 + c)u^2 - c^2(1 + c)\alpha^2)^2\beta^2 + 4c^4\alpha^4(x^4 + 2x^2(y^2 - \beta(\alpha + \beta)) + (y^2 + \beta^2)(y^2 + \beta(2\alpha + \beta)))^2}{(u^2 + c^2\alpha^2)^2(y^2 + (x - \beta)^2)^2(y^2 + (x + \beta)^2)^2}$$

$$n_{xy} = \frac{2(-1+c)xy\alpha((-1+c)u^4 - 2c^2(1+c)u^2\alpha^2 + c^4(3+c)\alpha^4)\beta(x^4 + 2x^2(y^2 - \beta(\alpha + \beta)) + (y^2 + \beta^2)(y^2 + \beta(2\alpha + \beta)))}{(u^2 + c^2\alpha^2)^2(x^2 + y^2 - 2x\beta + \beta^2)^2(x^2 + y^2 + 2x\beta + \beta^2)^2}$$

$$n_{yy} = \frac{64c^4x^2y^2\alpha^6\beta^2 + ((-1+c)u^2 - c^2(1+c)\alpha^2)^2(x^4 + 2x^2(y^2 - \beta(\alpha + \beta)) + (y^2 + \beta^2)(y^2 + \beta(2\alpha + \beta)))^2}{(u^2 + c^2\alpha^2)^2(y^2 + (x - \beta)^2)^2(y^2 + (x + \beta)^2)^2}$$

where u and v are given by Eq. (A6). When $c = 1$, through calculations, we find that $n_{xx} = n_{yy}$, $n_{xy} = 0$ and the refractive index returns to the isotropic result obtained through conformal mapping.

Appendix B. Geometric Ray Trajectories in Open-Ring Wormholes: A Transition Between Infinities

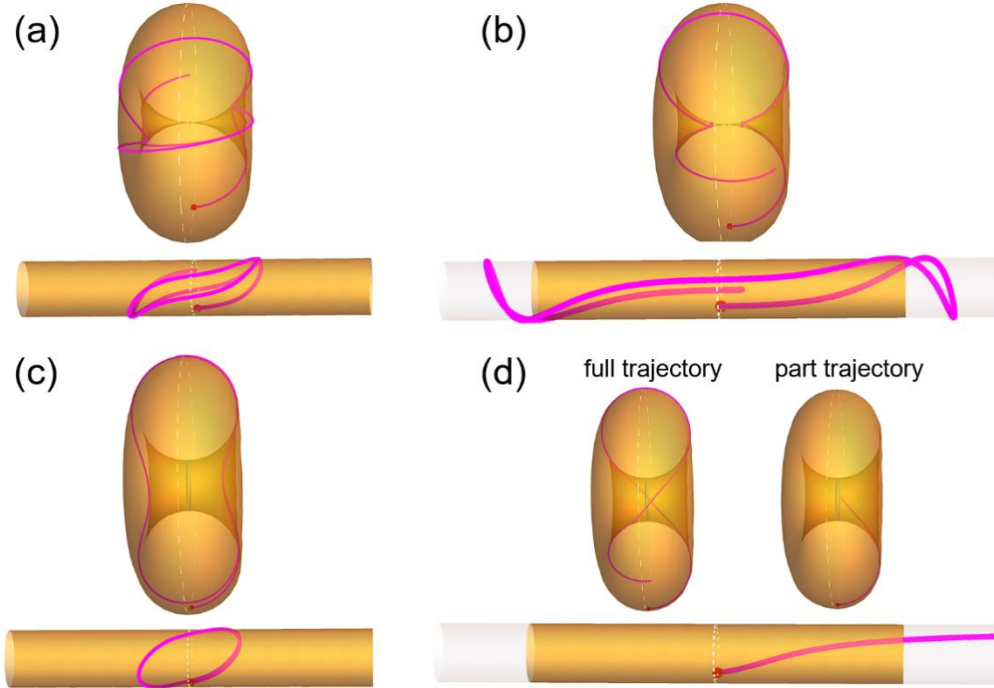


Fig. 5. Projection of the torus surface trajectory onto the cylindrical surface. (a) Ray trajectory at small angle incidence; (b) Ray trajectory at large angle incidence for the singularity of the horn-shaped torus. (c) Ray trajectory at small angle incidence; (d) Ray trajectory at large angle incidence for the throat (gray circle) of the ring torus. The red dots indicate the ray emission points.

This appendix primarily explains why the geometric ray trajectories of light trapped within an open-ring wormhole are inconsistent between virtual and physical spaces. When the light does not pass through infinity (i.e., the ends of the cylinder), as illustrated in Figs. 5 (a-c), the light follows a curved path due to the surface curvature of the ring, continuously circling around the ring. Through the torus projection described in the main text, we can project the complete trajectory of the ray on the ring to the cylindrical surface by filling the refractive index, as discussed in Section 3. This projection is shown on the cylindrical surface in the lower part of Figs. 5 (a-c). (To simplify our analysis, the light source is positioned at virtual-space coordinates (0,0)).

When $c = 1$, corresponding to a horn-shaped ring, due to the inherent structural properties of the ring's surface, no ray will pass through the singularity. Even rays that are incident directly towards the ring singularity will reverse their direction just before reaching the singularity, as

shown in Fig. 5(b). On the corresponding cylindrical diagram, the rays also turn back at a distant point on the cylinder.

However, when $c = 2/3$, and the rays do not pass through the interior of the ring, as shown in Fig. 5(c), the complete trajectory can still be represented correspondingly on the ring surface with the refractive index material. Once the rays pass through the interior of the ring, as shown in Fig. 5(d), the cylindrical surface fails to accurately reflect the complete trajectory of the rays within the ring. Instead, the rays are projected towards infinity. If we project rays near this infinity point back onto the ring surface, they will converge on an infinitesimally small circle centered at the gray region. This circle corresponds to the singularity where the horn-shaped wormhole is expanded.

To further clarify that this represents a transition from one infinity to another, we project the remaining ray trajectories from Fig. 6 (d) back onto the cylindrical surface, as shown in Fig. 6. As seen in Fig. 6(a), the red ray on the cylinder propagates to the right end; however, in Fig. S2(b), the ray propagates back from the left end of the cylinder. This indicates that the ray undergoes a transition at end, moving from one infinity to another. Furthermore, from Figs. 6 (b, c), the ray does not encounter the previous singularity, ensuring that the light remains continuous. From Figs. 6s (c, d), the ray again passes through the singularity where the ring expands, transitioning from one infinity to another. The complete trajectory on the ring, as well as the trajectory on the cylindrical surface with the material, is shown in Fig. 6(e).

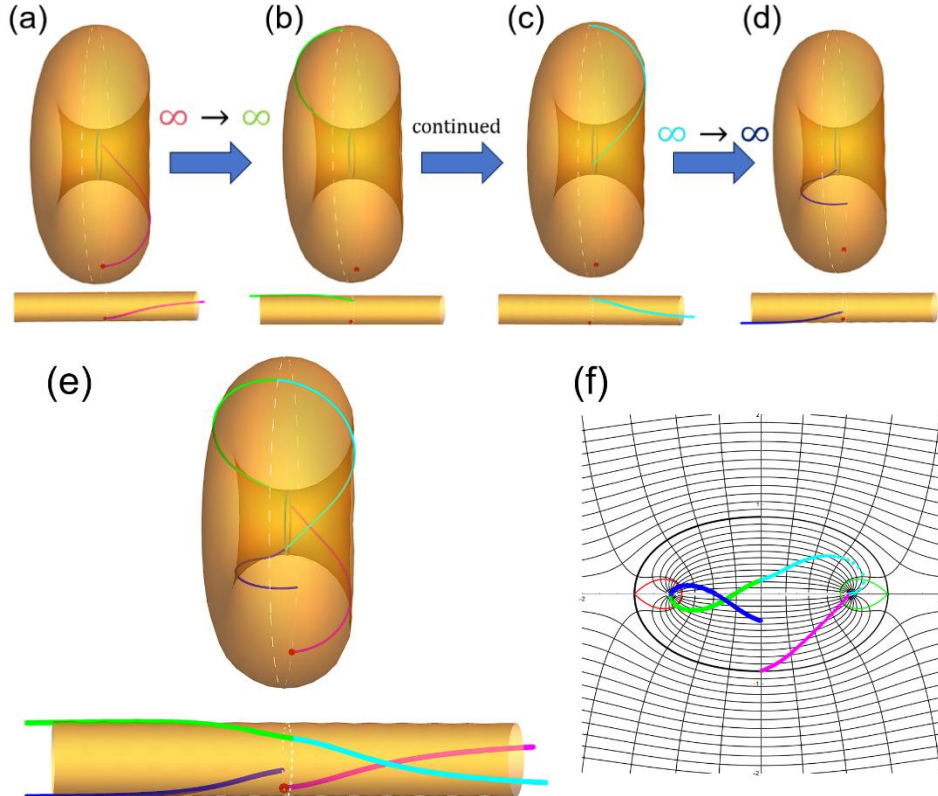


Fig. 6 Projection of the torus surface trajectory onto the cylindrical surface, experiencing a transition from infinity to infinity. Part trajectory of the ray for $\frac{\theta}{2}$ from (a) 0 to $\frac{\pi}{2}$ (b) $\frac{\pi}{2}$ to π (c)

π to $\frac{3\pi}{2}$ (d) $\frac{3\pi}{2}$ to 2π (e) Complete trajectory of the ray for $\frac{\theta}{2}$ from 0 to 2π . (f) Genetic Algorithm numerically reconstructed physical space trajectory.

This transition from one infinity to another is actually caused by the torus projection itself. As mentioned in the main text:

$$r' = R_2 \frac{\sin(\theta)}{\cos(\theta) + 1} \quad (B1)$$

By applying a simple half-angle transformation, we get:

$$r' = R_2 * \tan\left(\frac{\theta}{2}\right) \quad (B2)$$

When θ transitions from $\theta \rightarrow \pi^+$ to $\theta \rightarrow \pi^-$ (The ray passes through the gray circle), we observe that r' moves from $+\infty$ to $-\infty$. Therefore, this infinity-to-infinity transition can only be observed in the virtual space. In physical space, however, the light would become trapped at one of the infinities, akin to falling into a black hole. We can map the trajectory from virtual space to physical space by inversely solving for the spatial coordinates (x, y) through Eq. (A6). However, this coordinate inversion entails solving a nonlinear system. To address this, we numerically determine the solutions at discrete points, reconstructing the trajectory. As shown in Fig. 6(f), the resulting physical space trajectory exhibits a singularity-crossing transition from negative to positive infinity, analogous to the wormhole phenomenon depicted in only science fiction.

References

1. J. B. Pendry, D. Schurig, D. R. Smith, Controlling Electromagnetic Fields. *Science* **312**, 1780–1782 (2006).
2. U. Leonhardt, Optical Conformal Mapping. *Science* **312**, 1777–1780 (2006).
3. W. X. Jiang, C. Qiu, T. C. Han, Q. Cheng, H. F. Ma, S. Zhang, T. J. Cui, Broadband all-dielectric magnifying lens for far-field high-resolution imaging. *Adv. Mater.* **25**, 6963–6968 (2013).
4. Y. Kim, S.-Y. Lee, J.-W. Ryu, I. Kim, J.-H. Han, H.-S. Tae, M. Choi, B. Min, Designing whispering gallery modes via transformation optics. *Nat. Photonics* **10**, 647–652 (2016).
5. H. Chen, C. T. Chan, Electromagnetic wave manipulation by layered systems using the transformation media concept. *Phys. Rev. B* **78** (2008).
6. W. Cai, U. K. Chettiar, A. V. Kildishev, V. M. Shalaev, Optical cloaking with metamaterials. *Nat. Photonics* **1**, 224–227 (2007).
7. Y. Zhao, Y. Zhang, M. Zheng, X. Dong, X. Duan, Z. Zhao, Three-dimensional luneburg lens at optical frequencies. *Laser Photonics Rev.* **10**, 665–672 (2016).
8. Q. Ba, Y. Zhou, J. Li, W. Xiao, L. Ye, Y. Liu, J. Chen, H. Chen, Conformal optical black hole for cavity. *Elight* **2** (2022).
9. H. Chen, S. Tao, J. Bělín, J. Courtial, R.-X. Miao, Transformation cosmology. *Phys. Rev. A* **102**, 23528 (2020).
10. C. Sheng, H. Liu, Y. Wang, S. N. Zhu, D. A. Genov, Trapping light by mimicking gravitational lensing. *Nat. Photonics* **7**, 902–906 (2013).

11. D.-C. Dai, D. Minic, D. Stojkovic, How to form a wormhole. *Eur. Phys. J. C* **80**, 1103 (2020).
12. A. Einstein, N. Rosen, The particle problem in the general theory of relativity. *Phys. Rev.* **48**, 73–77 (1935).
13. A. Greenleaf, Y. Kurylev, M. Lassas, G. Uhlmann, Electromagnetic wormholes and virtual magnetic monopoles from metamaterials. *Phys. Rev. Lett.* **99**, 183901 (2007).
14. J. Zhu, Y. Liu, Z. Liang, T. Chen, J. Li, Elastic waves in curved space: mimicking a wormhole. *Phys. Rev. Lett.* **121**, 234301 (2018).
15. R. Q. He, G. H. Liang, S. N. Zhu, H. Liu, Simulation of giant tidal force of wormhole using curved optical spaces. *Phys. Rev. Res.* **2**, 13237 (2020).
16. I. Fernández-Núñez, O. Bulashenko, Anisotropic metamaterial as an analogue of a black hole. *Phys. Lett. A* **380**, 1–8 (2016).
17. R. A. Tinguely, A. P. Turner, Optical analogues to the equatorial kerr–newman black hole. *Commun. Phys.* **3** (2020).
18. H. Chen, R.-X. Miao, M. Li, Transformation optics that mimics the system outside a schwarzchild black hole. *Opt. Express* **18**, 15183 (2010).
19. L. Xu, H. Chen, Logarithm conformal mapping brings the cloaking effect. *Sci. Rep.* **4**, 6862 (2014).
20. L. Xu, H. Chen, T. Tyc, Y. Xie, S. A. Cummer, Perfect conformal invisible device with feasible refractive indexes. *Phys. Rev. B* **93**, 41406 (2016).
21. D. Schurig, J. B. Pendry, D. R. Smith, Calculation of material properties and ray tracing in transformation media. *Opt. Express* **14**, 9794 (2006).
22. J. C. Miñano, P. Benítez, A. Santamaría, Hamilton-jacobi equation in momentum space. *Opt. Express* **14**, 9083 (2006).
23. A. Frank, F. Leyvraz, K. B. Wolf, Hidden symmetry and potential group of the maxwell fish-eye. *J. Math. Phys.* **31**, 2757–2768 (1990).
24. U. Leonhardt, Perfect imaging without negative refraction. *New J. Phys.* **11**, 93040 (2009).
25. L. Xu, H. Chen, Conformal transformation optics. *Nat. Photonics* **9**, 15–23 (2015).
26. X. Wang, H. Chen, H. Liu, L. Xu, C. Sheng, S. Zhu, Self-focusing and the talbot effect in conformal transformation optics. *Phys. Rev. Lett.* **119**, 33902 (2017).
27. J. Wang, S. Valligatla, Y. Yin, L. Schwarz, M. Medina-Sánchez, S. Baunack, C. H. Lee, R. Thomale, S. Li, V. M. Fomin, L. Ma, O. G. Schmidt, Experimental observation of berry phases in optical möbius-strip microcavities. *Nat. Photonics* **17**, 120–125 (2023).
28. Y. Wang, Y. Ren, X. Luo, B. Li, Z. Chen, Z. Liu, F. Liu, Y. Cai, Y. Zhang, J. Liu, F. Li, Manipulating cavity photon dynamics by topologically curved space. *Light: Sci. Appl.* **11** (2022).

Acknowledgments: This work was supported by National Key Research and Development Program of China (Grant Nos. 2023YFA1407100 and 2020YFA0710100), National Natural Science Foundation of China (12404371), Jiangxi Provincial Natural Science Foundation (Grant

No. 20224ACB201005). Wen Xiao also acknowledges the support of China Postdoctoral Science Foundation (GZC20240906). Basic and Applied Basic Research Foundation of Guangdong Province (2024A1515011724)

Funding:

National Key Research and Development Program of China 2023YFA1407100

National Key Research and Development Program of China 2020YFA0710100

National Natural Science Foundation of China 12404371

Jiangxi Provincial Natural Science Foundation 20224ACB201005

Basic and Applied Basic Research Foundation of Guangdong Province
2024A1515011724

Competing interests: Authors declare that they have no competing interests.

Data and materials availability: All data are available in the main text or the supplementary materials.